Received: 24 June 2025 | Revised: 5 February 2026 | Accepted: 2 March 2026

DOI: 10.1111/jmi.70077

Journal of Microscopy RMS

ORIGINAL ARTICLE

Reduced order modelling of air-puff test for corneal material characterisation

Osama M. Maklad[1] | **Muting Hao**[2]

[1]Centre for Advanced Manufacturing and Materials, University of Greenwich, London, UK

[2]Oxford Thermofluid Institute, St John's College, University of Oxford, Oxford, UK

Correspondence
Osama M. Maklad, Centre for Advanced Manufacturing and Materials, University of Greenwich, London, UK.
Email: o.maklad@gre.ac.uk

Funding information
EPSRC National Fellowships in Fluid Dynamics (NFFDy) Summer programme 2024

Abstract

Models of the fluid–structure interaction (FSI) model for the air-puff test were analysed. Using Abaqus, the air-puff test is applied to eyes with varying biomechanical parameters, such as material properties, corneal thickness, and radius. A reduced order model of the air puff (a turbulent impinging jet) has been acquired to decrease simulation time from 48 h for the FSI model to approximately 12 min for the finite element analysis (FEA) model alone. To further accelerate simulations and improve model accuracy, Physics-Informed Neural Networks (PINNs) will be integrated with the reduced-order model. This hybrid approach will help expand the model to a larger dataset, enhancing intraocular pressure (IOP) estimation accuracy and the corneal material properties algorithm through inverse FEA. Additionally, a neural network (NN) framework with embedded Gaussian-modulated waveforms is proposed to model the pressure and deformation distributions on the corneal surface as functions of spatial and temporal parameters. By learning the relationship between corneal biomechanical inputs such as corneal central thickness (CCT), intraocular pressure (IOP), and baseline properties (μ), and the governing coefficients of pressure and deformation, the network accurately reconstructs the result that matches well with the high-fidelity CFD data. This approach can quickly capture the distribution of pressure and deformation. It can also provide insights into the distinct spatial and temporal dynamics of pressure and deformation, giving a more comprehensive understanding of fluid–structure interaction phenomena in the air-puff test.

KEYWORDS

air-puff test, fluid–structure interaction (FSI), Gradient Boosting Regressor (GBR), intraocular pressure (IOP), machine learning (ML), ocular biomechanics, reduced order modelling

1 | INTRODUCTION

In ophthalmology, the non-contact air-puff tonometry test is widely used to measure the biomechanical properties of the human cornea and intraocular pressure (IOP). Accurate IOP measurement is critical in evaluating patients at risk of eye diseases such as glaucoma, where elevated IOP can lead to optic nerve damage. Glaucoma is one of the leading causes of asymptomatic permanent blindness in the developed world. A common cause of IOP increase is the improper drainage of aqueous humour due to trabecular meshwork blockage.[1] The Ocular Response Analyser (ORA) was the first tonometry device that utilised an air puff to assess ocular biomechanical properties, using a dynamic infrared signal analysis.[2] Later, the Corvis-ST tonometer was developed, incorporating an ultra-high-speed Scheimpflug camera for better visualisation of corneal deformation.[3,4] The Corvis-ST applies a concentrated air puff to the centre of the cornea, deforming its geometry, which subsequently regains its original shape due to its elasticity. Using image processing, corneal deformation is recorded to estimate biomechanical properties and IOP through a programmed parametric equation.

Keratoconus, a degenerative eye disease, is characterised by the progressive thinning of the cornea, resulting in a cone-shaped protrusion.[5] This condition significantly alters the cornea's thickness, shape, and biomechanical properties[6], often causing irregular astigmatism and blurry vision. In patients with keratoconus, tonometry measurements of IOP tend to be lower due to the strong correlation between IOP readings and the altered biomechanical properties, particularly corneal central thickness (CCT).[7] Understanding these biomechanical changes is crucial for clarifying the pathophysiology and aetiology of keratoconus, aiding in its treatment.[8,9]

Accurate in vivo measurements of both IOP and corneal biomechanical parameters are essential. However, the challenge lies in the mutual dependence between these parameters, making it difficult to isolate the effects of IOP from biomechanical properties like thickness and material stiffness on corneal response.[3] Solving an inverse problem offers a potential solution to this challenge, allowing for a more accurate assessment of corneal material behaviour based on improved IOP values.[10,11]

The study of fluid–structure interaction (FSI) between the air puff and the cornea is necessary to address the correlation between IOP and corneal parameters and improve IOP estimation accuracy.[12–15] To achieve this, the air-puff pressure distribution profiles on the cornea must be considered when measuring corneal deformation.[12,16] The pressure exerted on the cornea dynamically changes in response to corneal deformation, which can alter clinical interpretations.[10,13,14] This effect termed the Corneal Load Alteration with Surface Shape (CLASS), highlights the importance of obtaining patient-specific air-puff pressure distributions.[13,17]

While the co-simulation of FSI has provided accurate values for pressure distribution and corneal deformation,[12–14,18] it remains time-consuming. The evolution of FSI approaches has led to precise estimations of air jet pressure changes with corneal characteristics, resulting in biomechanically corrected equations for accurate IOP and corneal material stress–strain indices.[11–13,17] However, predicting air-puff pressure in the computational fluid dynamics (CFD) model of FSI is computationally expensive, taking considerable time for patient-specific geometries. The primary goal of this study is to investigate how individual corneal characteristics affect air-puff pressure measurements and develop a machine learning (ML) algorithm to reduce computational costs. While numerical models of fluid flow are central to research on physical and mechanical phenomena, especially those involving FSI,[12–14] recent studies[19–21] suggest that ML can replace time-consuming numerical solvers, providing reduced-order models, improved optimisation, and lower computational costs.

To further improve the efficiency and accuracy of corneal response predictions, this study introduces a hybrid neural network (NN) with parametric embedding framework to model dynamic pressure and deformation distributions on the corneal surface. Observed patterns of pressure and deformation resemble Gaussian-modulated waveforms,[22,23] motivating the use of a parametric model characterised by five coefficients: amplitude (A), spatial scaling (β), temporal characteristics (μ and σ), and spatial attenuation (α). In this study, the NN is trained to map biomechanical input parameters—corneal central thickness (CCT), intraocular pressure (IOP), and baseline material properties (μ_0)—to these coefficients, enabling efficient reconstruction of pressure and deformation distributions. This approach accelerates computational workflows, replacing the need for expensive CFD simulations. It can also provide new insights into the spatial and temporal dynamics of corneal responses.

Therefore, this study is an extension to the authors' previous fluid–structure interaction (FSI) framework[12,13,18] by introducing a hybrid reduced-order modelling approach that integrates a Gradient Boosting Regressor (GBR) and a parametric neural network (NN) for pressure and deformation prediction during air-puff tonometry. The novelty of this work can be summarised as follows:

- Novel surrogate architecture: The GBR model is not a direct replacement of the CFD solver but a newly

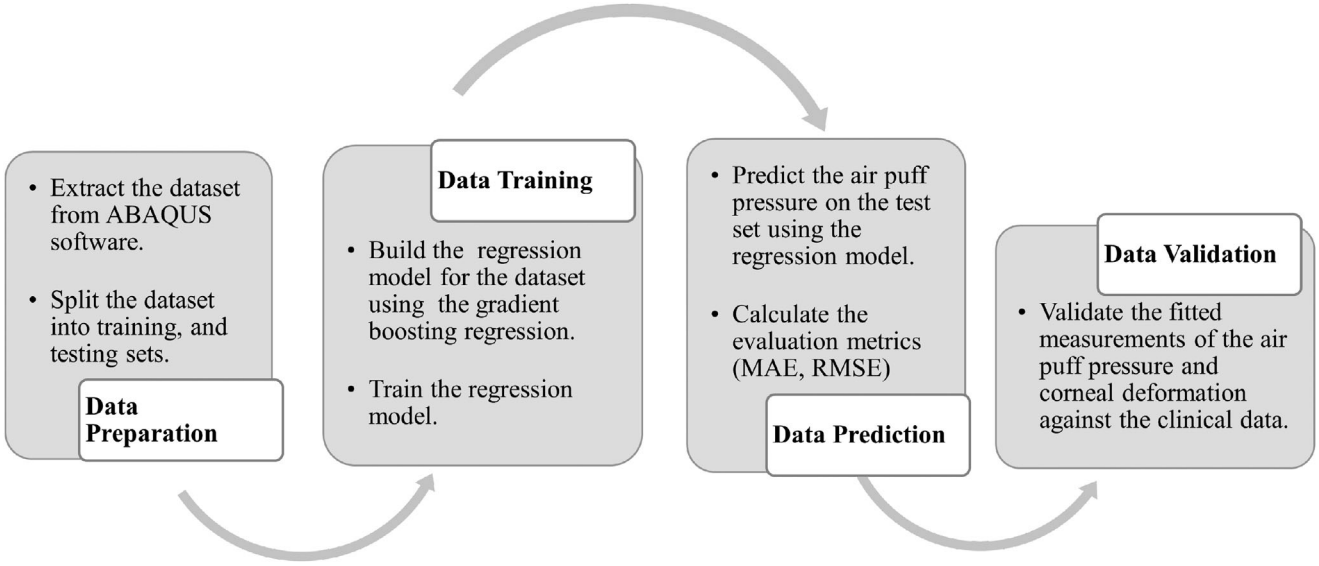

FIGURE 1 Flowchart of the data processing in the current study.

trained surrogate using FSI-generated data, enabling the decoupling of fluid and structural domains and reducing simulation time by ~ 99%.
- New NN embedding concept: The proposed parametric NN with Gaussian-modulated waveforms represents, to the best of our knowledge, the first use of such an interpretable neural architecture in modeling corneal pressure and deformation fields.
- Hybridisation of data-driven and physics-informed modelling: By combining GBR predictions of air-puff pressure with NN-based spatial–temporal reconstruction, this study introduces a scalable hybrid modelling framework that enhances physical interpretability and computational efficiency.
- Comparison with prior approaches: Unlike our earlier CFD-FSI model[13] and FE-only methods, the present model achieves equivalent accuracy with significantly lower computational demand.

This combination of model efficiency, interpretability, and clinical relevance represents a methodological advance toward real-time, patient-specific biomechanical assessment in air-puff tonometry.

2 | METHODS

This section outlines the dataset used in our approach and describes the algorithm applied for learning and prediction. We then explain the evaluation metrics used to assess the model's performance and conclude the section by presenting a validation study comparing the clinical data from patient cases with the outcomes of our algorithm. The data processing steps are illustrated in Figure 1, which will be elaborated upon in the subsequent sub-sections.

2.1 | Data collection and processing

This section details the dataset used as input to our algorithm, which was derived from the model of Ref. [20], involving a novel multi-physics, fully coupled fluid–structure interaction (FSI) model of the air-puff test of the Corvis ST on eye globes subjected to the internal load of IOP as shown in Figure 2B. These models were validated against clinical OCT images from the Corvis-ST device as shown in Figure 2A. Details of the numerical model, including, its validation and the used FSI two-way coupling approach with all the co-simulation control parameters and equations were published in our earlier study.[12,13,24] Here, we are giving the most important information, the air-puff was simulated using the turbulent Abaqus/CFD solver (version 6.14-2, Dassault Systèms Simulia Inc., USA) coupled with the finite element model of the eye using an arbitrary Lagrangian–Eulerian (ALE) deforming mesh. Models of the air domain consisted of six-nodded 3D fluid continuum elements (FC3D6) and used Spalart–Allmaras turbulent eddy viscosity model to simulate the turbulence in the air jet. To avoid excessive distortion of the air domain mesh during the coupling process with the eye model, an adaptive Arbitrary Lagrangian–Eulerian (ALE) deforming mesh was used to improve the stability of the simulation analysis. Due to the rotational symmetry of the parametric study results by Ref. [13,10] in both domains, a quarter of the two domains was simulated to reduce computational time. Figure 2B shows the

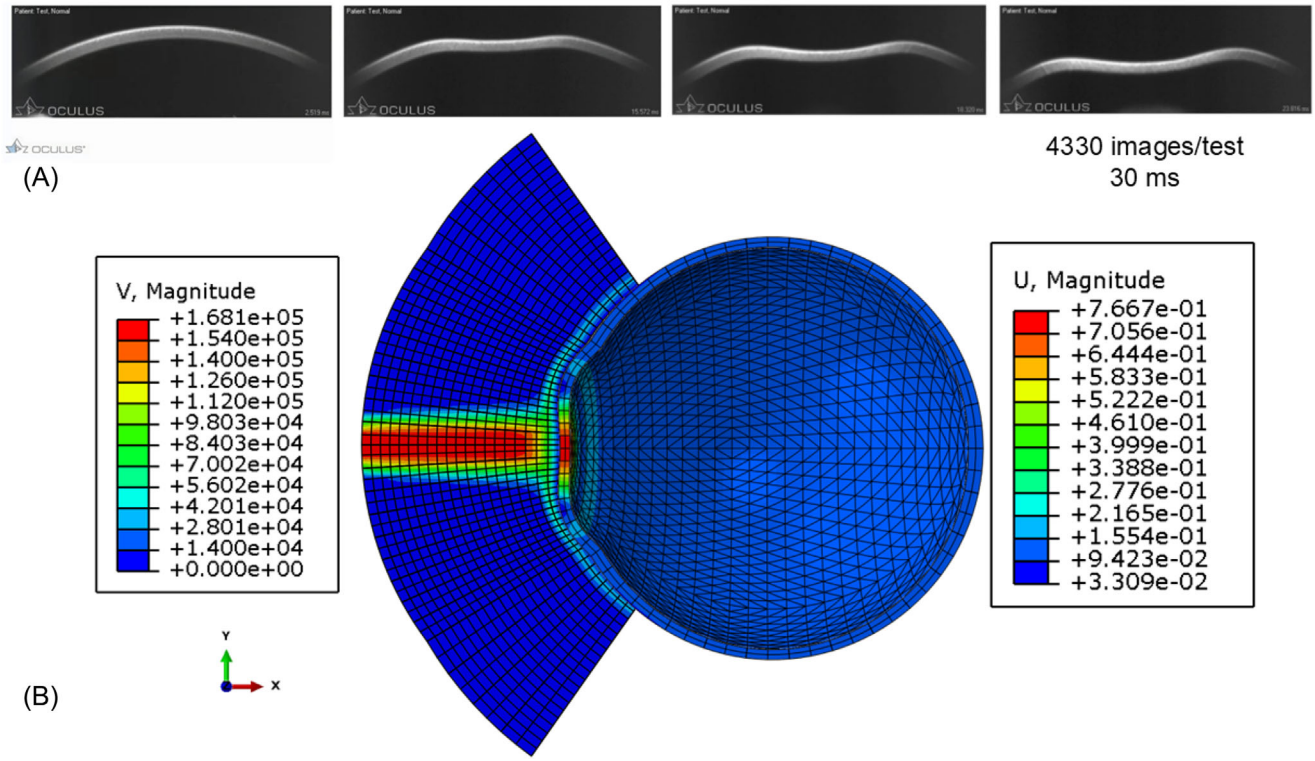

FIGURE 2 (A) The clinical optical coherence tomography images of the cornea under the air-puff test and (B) the FSI coupled model of the air-puff test in ABAQUS software.[13]

deformation values of the entire ocular vessel and the air-puff velocity values are indicated on the left (in mm/s), while the deformation values of the eye model are shown on the right (in mm).

This study considered three primary parameters: intraocular pressure (IOP), central corneal thickness (CCT), and the material stiffness coefficient (μ). The selection of five values for the material stiffness coefficient was based on the age-related relationship established by Ref. [25], where $\mu = 0.0328$ corresponds to an age of 30 years and $\mu = 0.1082$ corresponds to an age of 100 years. The effect of each parameter on the corneal pressure distribution was analysed while keeping the other parameters constant.

The dataset used to develop the regression model comprised 17 numerical simulations generated using the FSI model in ABAQUS 6.14,[13] along with ten clinical cases used for validation. The dataset contained both pressure distributions and corneal deformations, providing a comprehensive basis for training and evaluating the model.

The numerical simulations were structured as follows:

- First, the corneal pressure distribution was estimated for IOP values ranging from 10 to 25 mmHg, with a fixed CCT of 445 μm and a material stiffness coefficient of 0.0541.
- Next, the effect of varying CCT values (445, 495, 545, 595, and 645 μm) on the corneal pressure distribution was examined while maintaining an IOP of 15 mmHg and a material stiffness coefficient of 0.0541.
- Finally, the influence of different material stiffness coefficients (0.0328, 0.0541, 0.0683, 0.0811, and 0.1082) was analysed while holding the IOP at 15 mmHg and the CCT at 545 μm.

For each experiment, the dataset was divided into 70% for training, 20% for testing, and 10% for validation, ensuring robust model evaluation. The ten clinical cases were not included in the training phase but were used separately for overall validation. The model was trained to estimate the pressure distribution on the corneal surface, with accuracy evaluated using the Mean Absolute Error (MAE) metric, which quantifies the average absolute difference between the observed and predicted pressure values.

A summary of the corneal parameters used in the numerical dataset is presented in Table 1.

These parameters are independent and they don't have to be the same number of values, explaining the reason behind the chosen number of IOP samples (eight values) to reflect its strong non-linear effect on air-puff pressure response, whereas fewer increments were sufficient for CCT and material stiffness due to their smoother response behaviour in the tested range.

TABLE 1 Values of the corneal parameters used to train and test the regression model. Note that the number of parameter values differs because intraocular pressure (IOP) exhibits higher sensitivity to pressure–deformation dynamics, warranting denser sampling for model accuracy.

Parameter	Values (with units)							
IOP (mmHg)	10	13	15	17	20	22	24	25
CCT (μm)	445	495	545	595	645	—	—	—
μ (dimensionless)	0.0328	0.0541	0.0683	0.0811	0.1082	—	—	—

2.2 | The Gradient Boosting Regressor (GBR) algorithm

Gradient Boosting Machine (GBM) is a widely used machine learning algorithm for both regression and classification tasks. When applied to regression problems, this algorithm is referred to as the Gradient Boosting Regressor (GBR). The GBR approach relies primarily on three components: the loss function, the base learner, and an additive model structure.[23,26] In GBR, a series of tree-based models are constructed sequentially, with each subsequent model learning from the residuals (errors) of the previous one. By 'boosting' these weak learners—typically decision trees—into an ensemble, GBR creates a more robust and accurate predictive model.[23,26,27]

To effectively implement the GBR algorithm, several hyperparameters must be defined, as they significantly influence the model's performance and accuracy. In this study, we set the parameters as follows: squared-loss function, learning rate of 0.3, 2700 boosting stages, maximum tree depth of 6, and minimum samples required to split a node set to 5. The learning rate, a crucial parameter, determines how much each tree's prediction affects the final model. A lower learning rate slows the learning process but can enhance the model's stability and reliability.

The number of estimators (boosting stages) also plays an important role; generally, a higher number improves performance. The maximum depth parameter limits the depth of each decision tree, helping to prevent overfitting, while the minimum number of samples required to split a node influences the tree's branching structure.[27]

All computations were performed on an Intel Core i7 8550U processor with 8 GB RAM. Below, we detail the mathematical formulation of the GBR model.

Given an input x with prediction $\hat{y}$, the additive model of GBR can be formulated as follows:[27]

$$\hat{y} = \sum_{m=1}^{M} \gamma_m f_m(x),$$

where M represents the 'n_estimators' parameter, γ_m is the learning rate, and $f_m(x)$ is the base estimator (a weak learner).

The GBR algorithm is built iteratively, updating the model at each step. The updated model is given by:

$$\hat{y}^{(m+1)} = \hat{y}^{(m)} + \gamma_m f_m(x),$$

where each new tree $f_m(x)$ is fitted to minimise the sum of losses L over the previous ensemble:[27]

$$L = \sum_{i=1}^{n} \ell(y_i, \hat{y}_i^{(m)}).$$

Thus, for a given loss function ℓ, the model equation becomes:

$$\hat{y} = \hat{y}^{(0)} + \sum_{m=1}^{M} \gamma_m f_m(x).$$

By default, for a least-squares loss function, the initial prediction $\hat{y}^{(0)}$ is set to the mean of the target values. Using a first-order Taylor approximation, the incremental adjustment $f_m(x)$ can be approximated as:[27]

$$f_m(x) \approx -\frac{\partial L}{\partial \hat{y}^{(m)}},$$

where $-\frac{\partial L}{\partial \hat{y}^{(m)}}$ represents the negative gradient of the loss function. After removing constant terms, this results in:

$$f_m(x) = -\frac{\partial \ell(y, \hat{y})}{\partial \hat{y}}.$$

The algorithm continues iterating and updating gradients until it converges. This process can be seen as a form of gradient descent within a functional space.[27]

To evaluate the performance of the GBR model, we measured model error using Mean Absolute Error (MAE) and Root Mean Square Error (RMSE). The MAE, representing the average absolute difference between observed and predicted pressure values, is given by:

$$\text{MAE} = \frac{1}{n} \sum_{i=1}^{n} |y_i - \hat{y}_i|.$$

TABLE 2 Corneal parameters of the 10 clinical cases used in model validation.

Case ID (age, years)	IOP (mmHg)	CCT (μm)	μ (dimensionless)
Case 1 (73)	17.5	560	0.061
Case 2 (54)	18.0	579	0.054
Case 3 (63)	15.0	548	0.057
Case 4 (40)	24.0	582	0.051
Case 5 (53)	19.5	574	0.052
Case 6 (47)	17.0	566	0.0525
Case 7 (67)	16.0	553	0.058
Case 8 (80)	22.0	575	0.064
Case 9 (43)	25.0	533	0.0515
Case 10 (62)	16.5	576	0.056
Mean ± SD	**19.3 ± 3.4**	**564.6 ± 14.5**	**0.0558 ± 0.0043**

Similarly, RMSE, representing the standard deviation of prediction errors, is calculated as:

$$\text{RMSE} = \sqrt{\frac{1}{n}\sum_{i=1}^{n}(y_i - \hat{y}_i)^2}.$$

Additionally, we considered the computational time required for the model to train and generate predictions as an important factor due to our focus on reducing computational costs.

2.3 | Validation of the GBR algorithm

To validate our algorithm using clinical data, we utilised a diverse clinical dataset encompassing a range of corneal parameters from 10 healthy patients. This data was provided by the Vincieye Clinic in Milan, Italy, and the Rio de Janeiro Corneal Tomography and Biomechanics Study Group, Brazil. These clinical cases served as the input for the GBR algorithm, which was used to predict air-puff pressure loading and to compare with observed corneal deformations. Compliance with the ethical guidelines outlined in the Declaration of Helsinki (1964) and its 2013 revision was maintained, and all patients provided informed consent prior to the anonymised use of their data in this research. Details of the clinical cases included are summarised in Table 2.

Once the air-puff pressure loadings were predicted with the GBR algorithm, they were applied to the finite element (FE) model of the eye in ABAQUS 6-14. This three-dimensional eye model comprised 10,000 C3D15H continuum elements, each with 15 nodes and 9 integration points. These elements were arranged in two layers, spanning 15 rings along the cornea and 35 rings along the sclera. To stabilise the FE model, rigid body motion was restricted in the Z-direction at the equatorial nodes, while the posterior and anterior pole nodes were constrained in the X and Y directions, allowing free movement along the Z-axis, as illustrated in Figure 3. This configuration mirrors the setup used and validated in prior studies by the first author.[12,13,18]

2.4 | A hybrid neural network (NN) with parametric embedding framework of Gaussian-modulated waveforms

2.4.1 | Dataset and model validation

The dataset used to train the neural network consisted of 17 numerical simulation cases generated from the FSI model in ABAQUS,[12,18] each providing over one thousand time–space samples of pressure and deformation, resulting in approximately 17,000 total data points. The data were divided into 70% for training, 20% for testing, and 10% for validation to ensure robust model assessment. To check for overfitting, a fivefold cross-validation procedure was also applied during hyperparameter tuning. This ensures that the trained network generalises across different corneal parameter combinations (CCT, IOP, and μ_0).

2.4.2 | Overview of the neural network framework

This section proposes a neural network (NN) framework to model the pressure and deformation distributions on the corneal surface. Inspired by observed Gaussian-modulated wave patterns in experimental data, a parametric function was used to characterise the dynamics of pressure and deformation. This function, defined by five coefficients—amplitude (A), spatial scaling (β), temporal characteristics (μ and σ), and spatial attenuation (α)—forms the basis

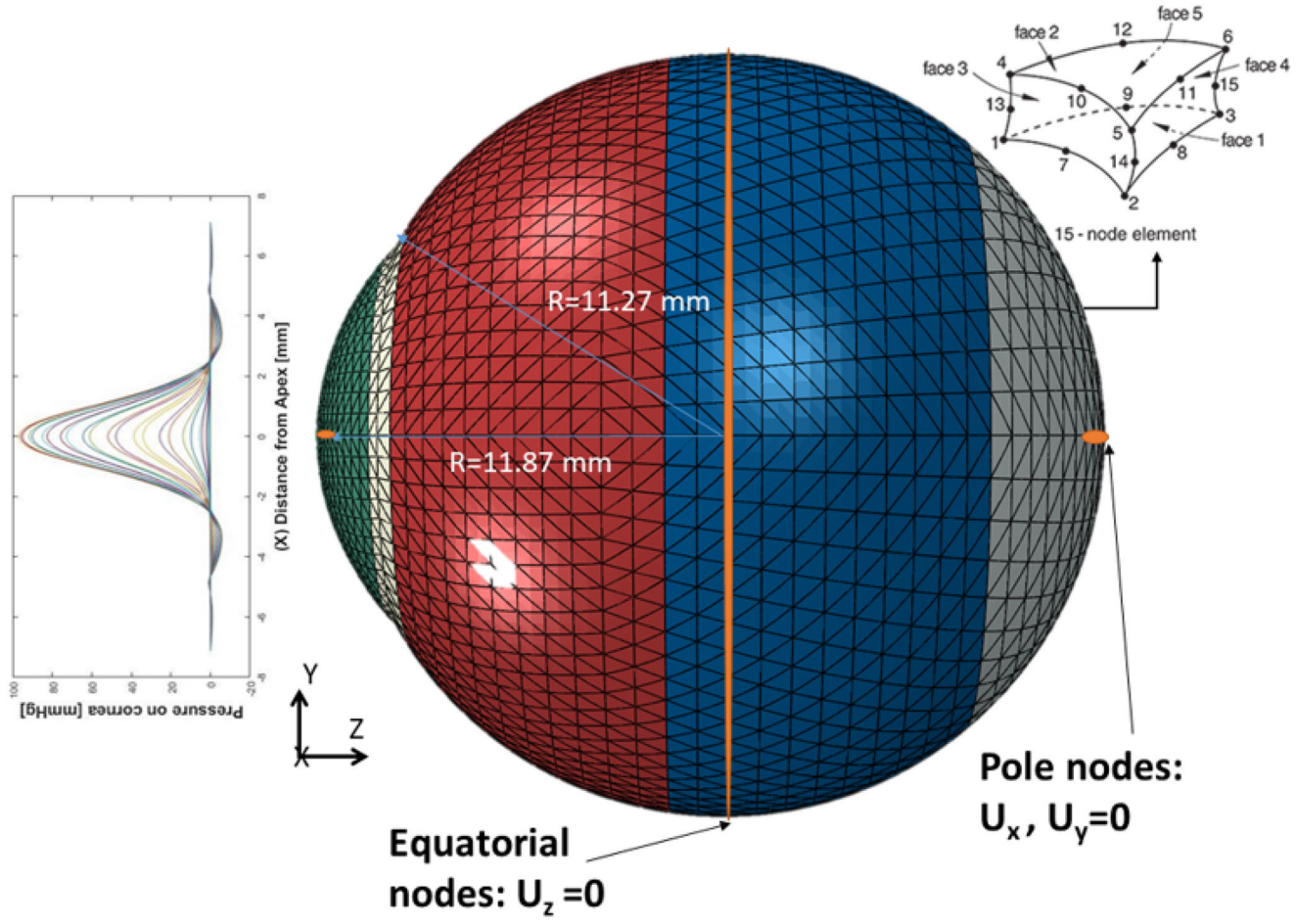

FIGURE 3 The finite element model of the eye with the boundary conditions.

for reconstructing pressure and deformation distributions. The NN is trained to map biomechanical inputs, including corneal central thickness (CCT), intraocular pressure (IOP), and baseline material properties (μ_0), to these coefficients.

2.4.3 | Parametric function for pressure and deformation

The dynamic behaviour of pressure and deformation is modelled using a Gaussian-modulated wave function, expressed as:

$$p_{\text{pred}}, dz_{\text{pred}} = A \cdot (1 - \alpha \cdot \beta \cdot x^2) \cdot \exp(-\beta \cdot x^2) \cdot \exp\left(-\frac{(t-\mu)^2}{2\sigma}\right), \quad (1)$$

where p_{pred}, dz_{pred} represents the predicted pressure or deformation using NN at cornea spatial position coordinate x and time t. Five coefficients are additionally included: A is the amplitude of the pressure or deformation wave, α is the coefficient controlling spatial attenuation, β is the spatial scaling parameter, μ is the temporal mean indicating the centre of the wave and σ is the temporal standard deviation, determining the wave spread. These coefficients capture both spatial and temporal dynamics and support the reconstruction of the distributions. p_{pred} and dz_{pred} follow the same function as Equation 1 but with different values of coefficients.

2.4.4 | Neural network architecture

The NN framework is designed to map input parameters (CCT, IOP, μ_0) to the output coefficients (A, α, β, μ, σ). Table 3 summarises the network architecture. The input layer has three nodes representing CCT, IOP, and μ_0. Hidden layers are two fully connected layers with 64 neurons each, employing ReLU (Rectified Linear Unit) activation to introduce non-linearity. The output layer includes five neurons, each representing one of the parametric

TABLE 3 Neural network architecture.

Layer	Number of neurons	Activation function
Input Layer	3	—
Hidden Layer 1	64	ReLU
Hidden Layer 2	64	ReLU
Output Layer	5	Linear

coefficients (A, α, β, μ, σ). A linear activation function is used for the output layer to allow unrestricted values.

2.4.5 | Loss function

The loss function is designed to minimise the mean squared error (MSE) between the predicted and actual pressure or deformation values. Taking pressure for example:

$$\text{Loss} = \frac{1}{N}\sum_{i=1}^{N}\left(p_{\text{pred},i} - p_{\text{true},i}\right)^2, \tag{2}$$

where N is the total number of samples, $p_{\text{pred},i}$ is the predicted pressure, and $p_{\text{true},i}$ is the ground truth.

2.4.6 | Gradient derivations for backpropagation

To update the NN weights using backpropagation, the gradient of the loss function with respect to each parametric coefficient is explicitly derived as follows:

$$\frac{\partial \text{Loss}}{\partial A} = \frac{2}{N}\sum_{i=1}^{N}(p_{\text{pred},i} - p_{\text{true},i}) \cdot (1 - \alpha \cdot \beta \cdot x^2) \cdot \exp(-\beta \cdot x^2) \cdot \exp\left(-\frac{(t-\mu)^2}{2\sigma^2}\right). \tag{3}$$

$$\frac{\partial \text{Loss}}{\partial \alpha} = -\frac{2}{N}\sum_{i=1}^{N}(p_{\text{pred},i} - p_{\text{true},i}) \cdot A \cdot \beta \cdot x^2 \cdot \exp(-\beta \cdot x^2) \cdot \exp\left(-\frac{(t-\mu)^2}{2\sigma^2}\right). \tag{4}$$

$$\frac{\partial \text{Loss}}{\partial \beta} = \frac{2}{N}\sum_{i=1}^{N}(p_{\text{pred},i} - p_{\text{true},i}) \cdot A \cdot \left[(\alpha \cdot x^2 - x^2) \cdot \exp(-\beta \cdot x^2)\right] \cdot \exp\left(-\frac{(t-\mu)^2}{2\sigma^2}\right). \tag{5}$$

$$\frac{\partial \text{Loss}}{\partial \mu} = \frac{2}{N}\sum_{i=1}^{N}(p_{\text{pred},i} - p_{\text{true},i}) \cdot A \cdot (1 - \alpha \cdot \beta \cdot x^2) \cdot \exp(-\beta \cdot x^2) \cdot \frac{t-\mu}{\sigma^2} \cdot \exp\left(-\frac{(t-\mu)^2}{2\sigma^2}\right). \tag{6}$$

$$\frac{\partial \text{Loss}}{\partial \sigma} = \frac{2}{N}\sum_{i=1}^{N}(p_{\text{pred},i} - p_{\text{true},i}) \cdot A \cdot (1 - \alpha \cdot \beta \cdot x^2) \cdot \exp(-\beta \cdot x^2) \cdot \frac{(t-\mu)^2}{\sigma^3} \cdot \exp\left(-\frac{(t-\mu)^2}{2\sigma^2}\right). \tag{7}$$

2.4.7 | Training configuration

Each data point in the dataset corresponds to a unique combination of spatial position (x) and time (t), treated as a separate instance with its associated input parameters: corneal central thickness (CCT), intraocular pressure (IOP), and baseline material property (μ_0). These three parameters serve as the inputs to the neural network.

The NN was optimised using the Adam optimiser, with an initial learning rate of 0.0005 and decay rate $1e-3$. The model was trained for 10,000 epochs.

3 | RESULTS

3.1 | Estimation of the air pressure distribution on the cornea

To examine the impact of corneal parameters on the air-puff pressure distribution, we assessed the Gradient Boosting Regressor (GBR) model's performance in predicting changes in corneal pressure distribution under varying conditions. Initially, the effect of intraocular pressure (IOP) variations on estimated pressure distribution was evaluated. Pressure distribution on the corneal surface was obtained for eight IOP values (10, 13, 15, 17, 20, 22, 24, and 25 mmHg), while keeping the central corneal thickness (CCT) constant at 445 μm and a material stiffness coefficient set at 0.0541. The fitted GBR model demonstrated strong alignment with the numerical values from the fluid–structure interaction (FSI) model, yielding a mean absolute error (MAE) of 0.0212, root mean square error (RMSE) of 0.0682, and an execution time of 12 s.

Then, the effect of CCT variations (445, 495, 545, 595, and 645 μm) on corneal pressure distribution was assessed at an IOP of 15 mmHg and a material stiffness coefficient of 0.0541. The GBR algorithm again aligned closely with the ABAQUS numerical model, with MAE = 0.0171, RMSE = 0.0578, and an execution time of 10 s. Finally,

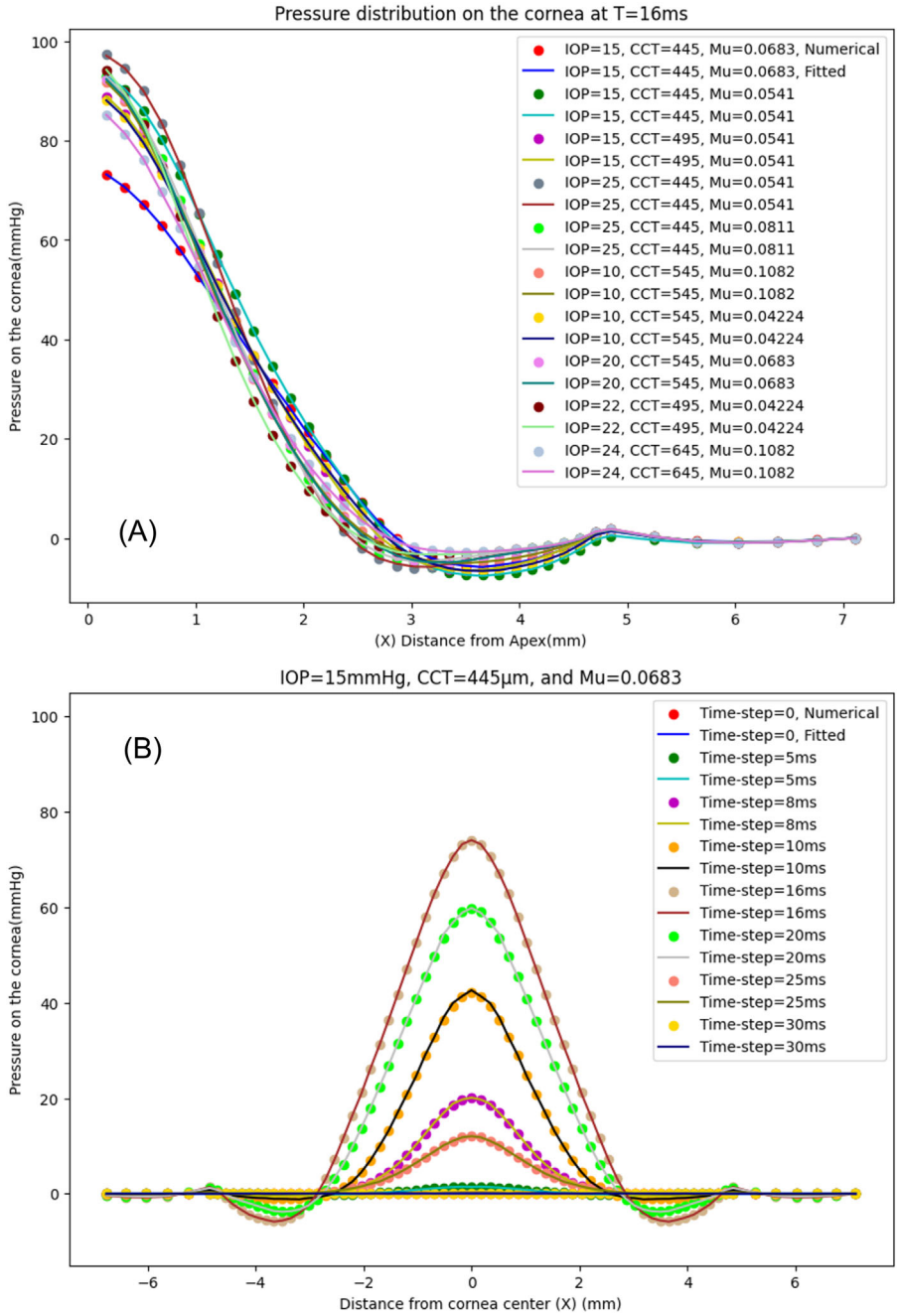

FIGURE 4 (A) Comparison between the numerical ABAQUS CFD–FSI model and the fitted GBR algorithm for pressure distribution on the corneal surface at $t = 16$ ms under different corneal parameters: intraocular pressure (IOP), central corneal thickness (CCT), and stiffness coefficient (μ). (B) Temporal evolution of pressure distribution for the baseline case (IOP = 15 mmHg, CCT = 445 μm, $\mu = 0.0683$). Axes: radial distance (mm) and pressure (mmHg). Symbols are the numerical model values and solid lines are the GBR algorithm fitting.

the influence of material stiffness coefficient variations, representing age-related stiffness changes (0.0328, 0.0541, 0.0683, 0.0811, and 0.1082), was examined at an IOP of 15 mmHg and CCT of 545 μm. The GBR model produced highly accurate pressure distributions, with an MAE of 0.0113, RMSE of 0.0491, and an execution time of 12 s.

The pressure profile results, shown in Figure 4A, indicate that modifying a single corneal parameter can alter the entire pressure profile, while Figure 4B illustrates the temporal pressure distribution across the cornea.

The algorithm demonstrated strong alignment with the numerical model, achieving a mean absolute error (MAE) of 0.0258, root mean square error (RMSE) of 0.0673, and an execution time of 10–12 s. The results reveal no consistent pattern between changes in air-puff pressure loading and individual parameters, as the pressure distribution on the

TABLE 4 RMSE of air-puff pressure loading predicted by the GBR algorithm for different corneal parameters varied independently.

IOP (mmHg)		CCT (μm)		μ (dimensionless)	
Value	**RMSE**	**Value**	**RMSE**	**Value**	**RMSE**
10	0.0186	445	0.0322	0.0328	0.0201
13	0.0453	495	0.1021	0.0541	0.0340
15	0.0511	545	0.0467	0.0683	0.0119
17	0.0530	595	0.0458	0.0811	0.0362
20	0.0769	645	0.0759	0.1082	0.0533
25	0.0894	—	—	—	

cornea is influenced by all parameters collectively, highlighting the importance of considering them in tandem to achieve accurate air-puff pressure predictions, as reflected in Table 4. The results indicate that peak pressure at the corneal apex varies across the two models, with higher values observed for lower IOP cases, thicker corneas, and stiffer corneas. These outcomes underscore the GBR model's capacity to accurately capture patient-specific corneal parameter variations for different cases.

3.2 | Validation of the GBR algorithm

To clinically validate the proposed algorithm, a dataset containing a diverse range of corneal parameters for 10 healthy patients was used. Following air-puff pressure predictions generated by the GBR algorithm, these predictions were applied to the finite element (FE) only model of the eye in `ABAQUS 6-14`. The FE model required about 10 min to process and produce corneal deformation results from the predicted air-puff pressures. These deformation results were then compared with clinical deformation data to complete the validation process. This approach serves as an efficient alternative to the traditional CFD model by significantly reducing computational time, from approximately 48 h (172,800 s) in the FSI model to just 12 min (720 s), achieving about a 99.2% reduction in runtime; see Table 5 for comparison.

Figure 5 illustrates the temporal comparison of apical deformation against clinical data, while Figure 6 compares spatial corneal deformations based on the predicted air-puff loading. Figure 7 presents the comparison of the temporal pressure profiles, demonstrating that the GBR model provides a close estimation of the normalised pressure distribution at the corneal centre, as indicated by the calculated RMSE between the clinical data and model predictions. Furthermore, the numerical FSI results are included to show that the GBR algorithm can achieve comparable or improved accuracy in estimating the pressure load while significantly reducing computational time. These comparisons demonstrate that the algorithm reliably replicates the actual corneal behaviour. It's important to note that what matters most here is the agreement between the GBR algorithm and the numerical model results which it was trained on. The less agreement with the clinical behaviour is more related to the limitations of the numerical model which was mentioned in [12,13,18], mainly related to the idealised material model and assumptions made in the boundary conditions.

Furthermore, to assess the improvement achieved by integrating the GBR algorithm with the FE model over using the FE model alone for apical deformation predictions, RMSE values were calculated for both methods, with results presented in Table 6.

To quantify the variability in model predictions, each GBR simulation was repeated five times using different random seeds and data partitions. The resulting error metrics (MAE and RMSE) were averaged across runs, and the corresponding standard deviations were reported to reflect the statistical variation. For clinical validation, 95% confidence intervals (CIs) were computed using the Student's *t*-distribution to indicate uncertainty in model performance across the ten test cases. These CIs are presented in Table 6.

The inclusion of standard deviations and confidence intervals highlights the stability of the GBR predictions across repeated trials. The narrow variation range (±0.01) indicates consistent model performance despite small perturbations in data partitioning. However, as the clinical

TABLE 5 Comparison between the current study and previous modelling approaches for simulating air-puff tests.

Model type	Description	Computational Time	Accuracy (RMSE)	Key Advantage	Reference
CFD–FSI	Fully coupled Abaqus CFD–FE co-simulation of air-puff test	~48 h	0.05–0.08	High fidelity but computationally expensive	[13]
FE-only	Finite element deformation model with empirically prescribed air-puff pressure	~10 min	0.10–0.15	Faster but lacks pressure feedback	[10]
Proposed GBR + NN hybrid	Surrogate GBR predicts air-puff pressure; NN reconstructs pressure and deformation distributions	**~12 min**	**0.05–0.07**	~99% faster; interpretable; clinically scalable	**This study**

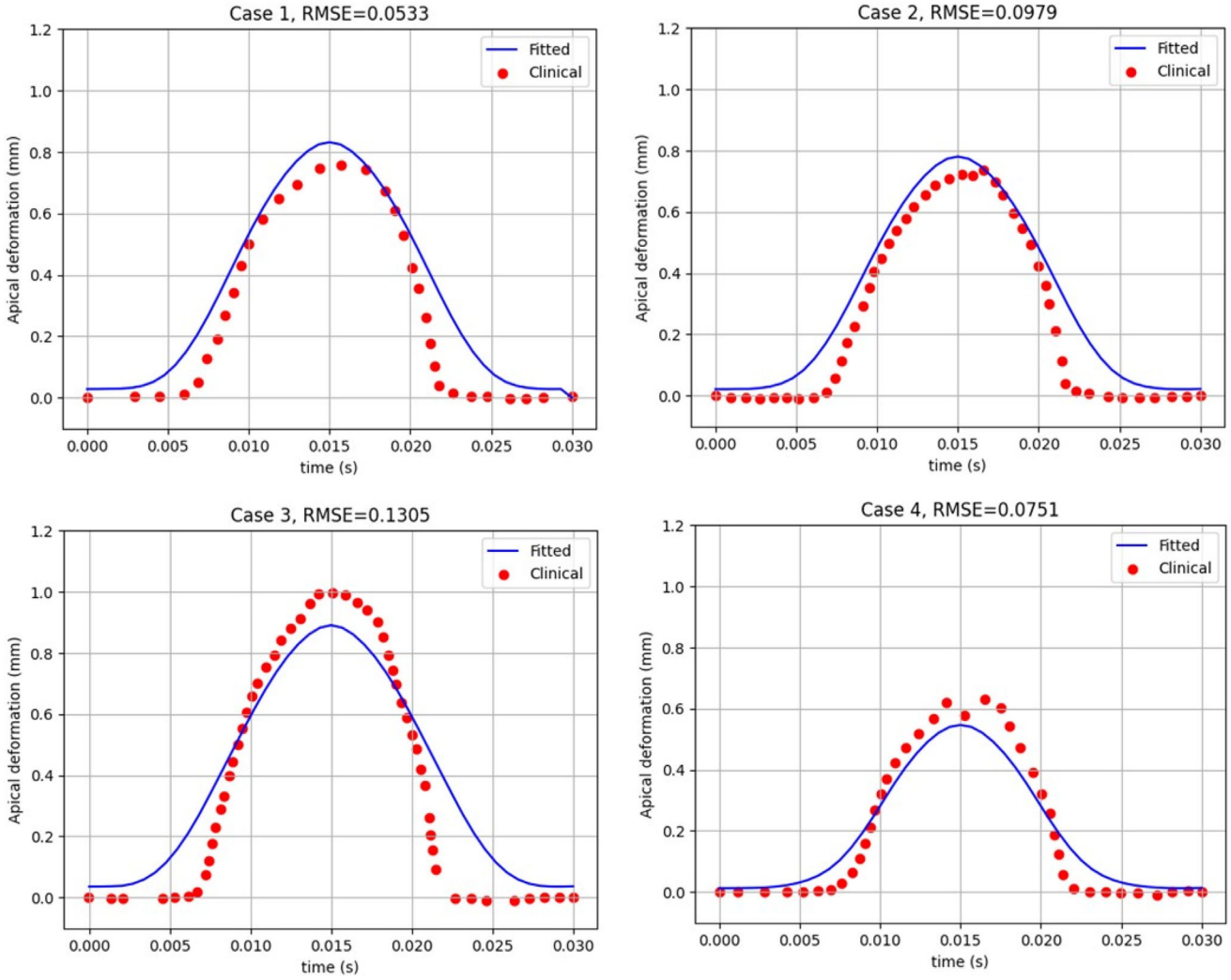

FIGURE 5 Comparison of apical deformation over time between the GBR+FE model predictions and clinical measurements for four representative cases with distinct corneal parameters (see Table 2). Symbols are the clinical apical deformations, and solid lines are for the GBR algorithm.

TABLE 6 RMSE between predicted and clinically observed apical deformations for ten cases. Each RMSE value represents the mean ± standard deviation across five independent runs. The GBR + FE hybrid model consistently achieves lower RMSE compared to the FE-only model, confirming improved prediction accuracy.

Clinical case	GBR + FE model vs. clinical (RMSE)	FE model only vs. clinical (RMSE)
Case 1	0.0612 ± 0.008	0.5784 ± 0.021
Case 2	0.0865 ± 0.010	0.4214 ± 0.017
Case 3	0.1203 ± 0.011	0.4854 ± 0.022
Case 4	0.0814 ± 0.009	0.3625 ± 0.019
Case 5	0.0736 ± 0.007	0.3982 ± 0.018
Case 6	0.0679 ± 0.008	0.4373 ± 0.020
Case 7	0.0958 ± 0.010	0.4167 ± 0.021
Case 8	0.0881 ± 0.009	0.4562 ± 0.019
Case 9	0.0795 ± 0.008	0.5031 ± 0.022
Case 10	0.0717 ± 0.007	0.4748 ± 0.020
Average (95% CI)	**0.0826 [0.068, 0.097]**	**0.453 [0.392, 0.514]**

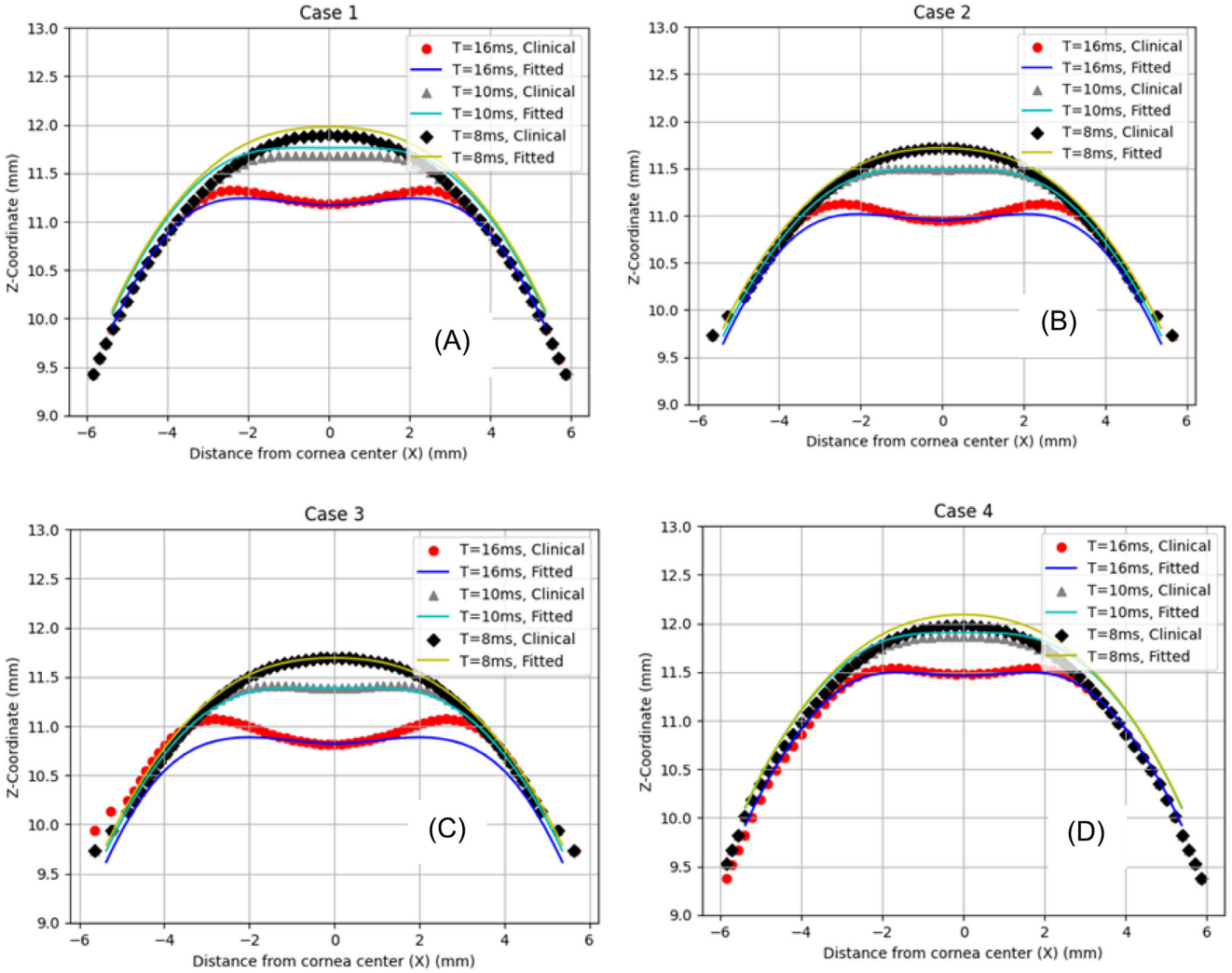

FIGURE 6 Comparison of spatial corneal deformation patterns between GBR+FE model predictions and clinical data for four representative cases. Symbols are the clinical deformations, and solid lines are for the GBR algorithm. Agreement across cases demonstrates reliable reproduction of observed deformation trends.

validation set comprised only 10 eyes, further work will expand this analysis to a larger and more diverse patient population to better assess generalisation and robustness. Future datasets will include eyes with pathological conditions such as keratoconus to test performance beyond healthy corneas.

3.3 | Results of the neural network method

Figure 8 presents the comparison between predicted and original pressure (P) and deformation (dz) distributions on the corneal surface as functions of spatial position (X) and time (t) for six representative cases. Each subfigure includes four 3D surfaces: the CFD original pressure (P_{original}, green), NN-predicted pressure (P_{predict}, purple), CFD original deformation (dz_{original}, orange), and NN-predicted deformation (dz_{predict}, blue). Figures 9 and S1 and the videos in the Supplementary Material show the temporal pressure and deformation profiles for a representative case proving the accuracy of the algorithm. The agreement between the NN-predicted and CFD original surfaces demonstrates the accuracy of the proposed neural network in reconstructing both pressure and deformation distributions.

The results reveal that the temporal variations of pressure and deformation are similar, as indicated by their coefficients μ (temporal mean) and σ (temporal standard deviation). This similarity suggests shared temporal dynamics for pressure and cornea deformation. However, significant differences are observed in the spatial patterns, governed by coefficients A, α, and β. Specifically, A for deformation has an opposite sign and a smaller magnitude

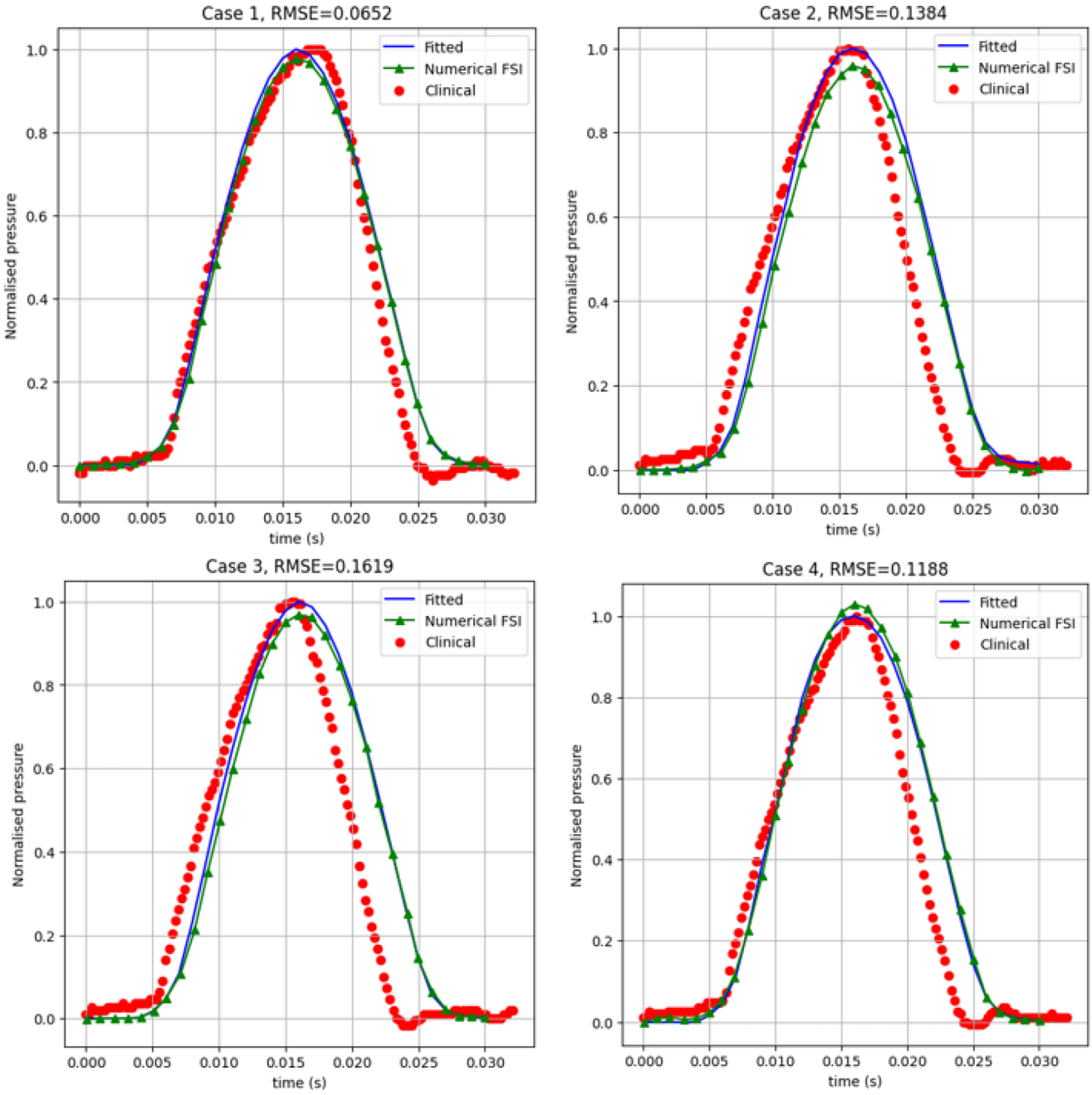

FIGURE 7 Comparison of the air-puff pressure profiles on cornea centre clinically, numerically, and predicted from the GBR algorithm for four representative cases. Red dots are the clinical pressure profile, and blue solid lines are for the GBR algorithm while the green lines are the CFD model pressure profile. Agreement across cases demonstrates reliable reproduction of observed deformation trends.

compared to A for pressure, with $A_{\text{deformation}} \approx -0.01 \cdot A_{\text{pressure}}$. These distinctions highlight the different spatial attenuation and scaling behaviours of pressure and deformation, with deformation exhibiting less steeper spatial variability. Figure 1 demonstrates that the NN with the proposed wavelet function accurately and efficiently captures both shared temporal and distinct spatial characteristics of pressure and deformation.

Figure 10 illustrates the correlations between the input parameters (CCT, IOP, μ_0) and the output coefficients (A, α, β, μ, σ) for both pressure and deformation. Each subplot shows scatterplots with fitting lines to describe the correlation.

The five learnt coefficients (A, α, β, μ, σ) have clear physical interpretations consistent with the underlying mechanics of the air-puff test: A represents the amplitude of the pressure or deformation response; α controls spatial attenuation, describing how rapidly the response decays radially; β defines spatial scaling, related to curvature and stiffness effects; μ corresponds to the temporal mean,

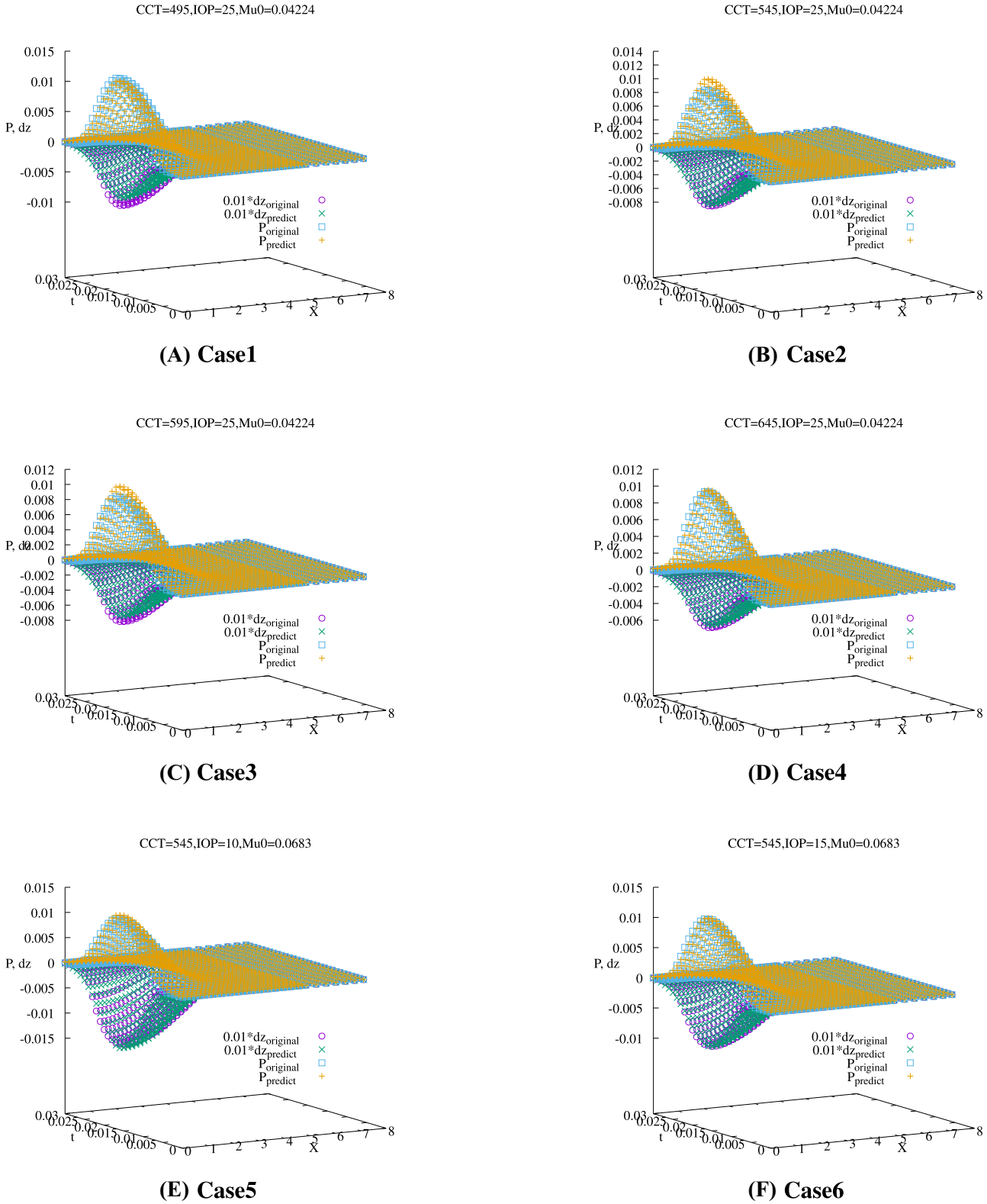

FIGURE 8 Comparison between CFD reference data and NN-predicted pressure (P) and deformation (dz) distributions across space (X in mm) and time (t in s) for six representative cases. Green: CFD pressure $P_{original}$; purple: NN-predicted pressure $P_{predict}$; orange: CFD deformation $dz_{original}$; blue: NN-predicted deformation $dz_{predict}$.

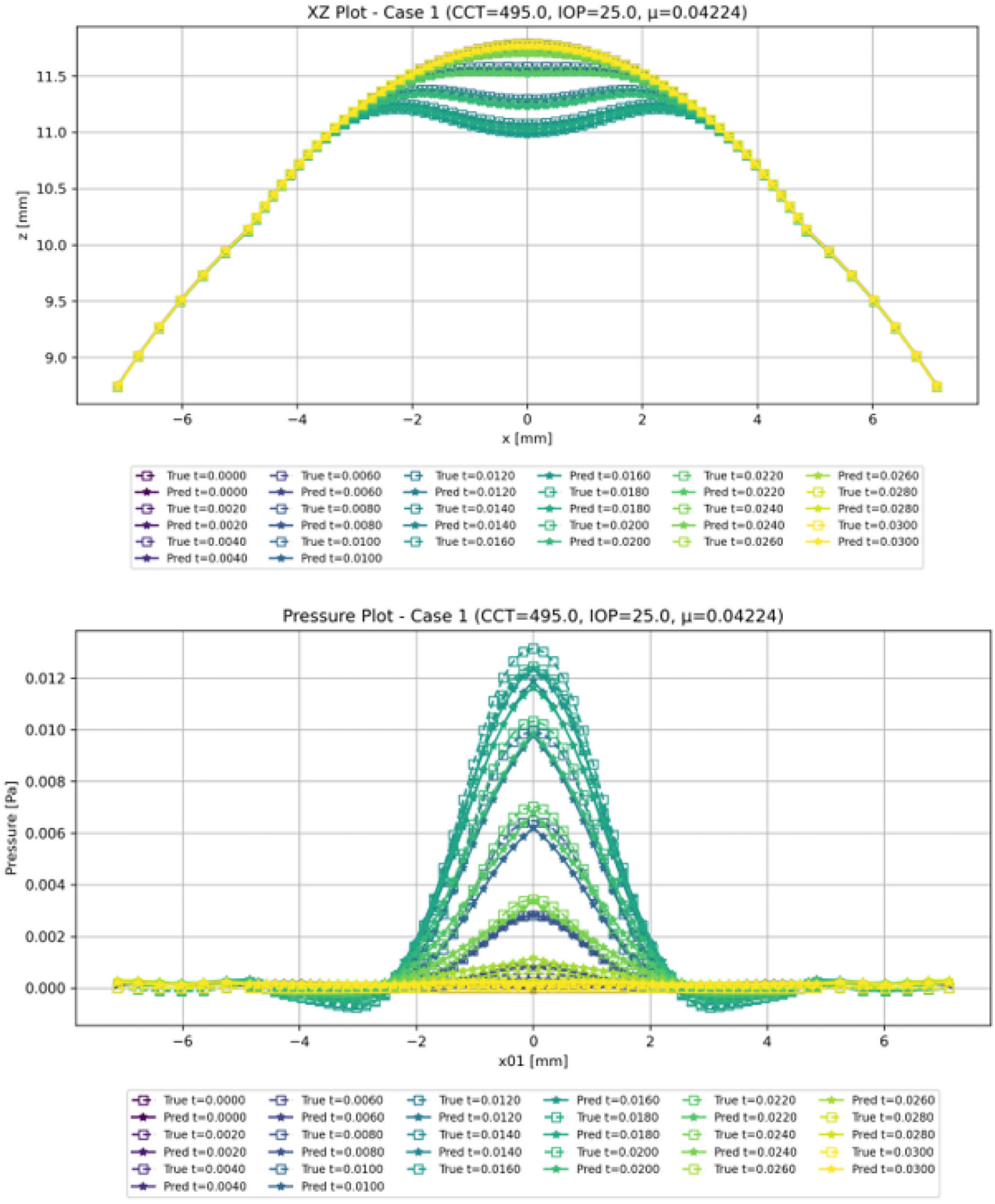

FIGURE 9 Comparison between CFD reference data and NN-predicted temporal pressure (P) and deformation (dz) distributions across space (X in mm) and time (t in s) for a representative case. Solid lines CFD pressure or deformations; symbols: NN-predicted values.

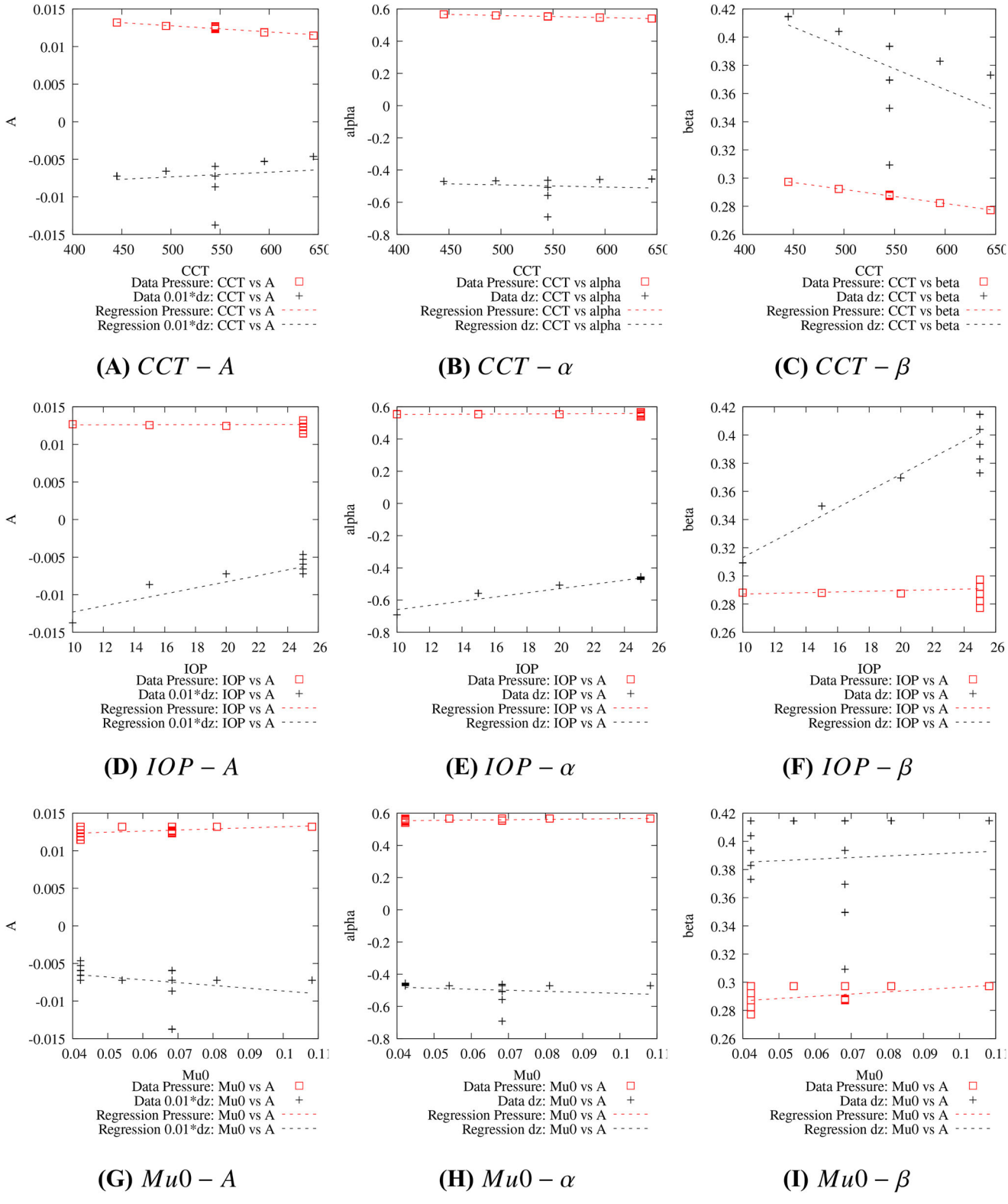

FIGURE 10 Relationships between biomechanical inputs (CCT, IOP, μ_0) and learnt parametric coefficients (A, α, β, μ, σ) for pressure and deformation. Each subplot shows scatter data with linear regression fits. These correlations highlight the physical interpretability of the NN coefficients.

representing the time of maximum response; and σ governs temporal spread, reflecting the duration of corneal recovery. By correlating these coefficients with biomechanical inputs (Figure 10), the network provides physically interpretable mappings rather than purely empirical fitting.

The analysis indicates that pressure and deformation exhibit different dependencies on the input parameters. For instance, A_{pressure} correlates positively with IOP, while $A_{\text{deformation}}$ shows a negative correlation with CCT. Temporal coefficients μ and σ demonstrate minor correlations with all inputs, reflecting shared temporal influences between pressure and deformation. In contrast, spatial coefficients α and β exhibit high sensitivity to inputs CCT, IOP and slightly lower to μ_0, with β_{pressure} strongly influenced by CCT, whereas $\beta_{\text{deformation}}$ depends more on CCT and IOP. This parametric modeling shows consistency for pressure and deformation. Figure 10 demonstrates the relationships between corneal fluid–solid interaction and the observed pressure and deformation distributions.

Model performance was quantitatively assessed using three standard regression metrics: mean absolute error (MAE), root mean square error (RMSE), and the coefficient of determination (R^2). The average values over all test cases were MAE $= 0.018$, RMSE $= 0.052$, and $R^2 = 0.97$, indicating excellent agreement between the NN predictions and the high-fidelity CFD reference data. These metrics correspond to the pressure and deformation surface plots presented in Figure 8, where both temporal and spatial distributions were reconstructed from the learned parameters.

4 | LIMITATIONS AND FUTURE WORK

Although the proposed GBR–NN hybrid framework achieved significant reductions in computational time and demonstrated close agreement with CFD–FSI and clinical data, several limitations must be acknowledged.

First, the data set used to train machine learning models was derived from 17 numerical simulations and 10 clinical cases. Although these covered a representative range of corneal parameters (IOP, CCT and μ_0), a larger and more diverse data set is required to fully capture interpatient variability and pathological conditions such as keratoconus.

Second, the current model assumes axisymmetric corneal geometry, isotropic material, and uniform air jet alignment, which simplifies the underlying physics but may limit generalisation to off-axis or asymmetric dynamic corneal topographies. Future work will incorporate full three-dimensional eye geometries and patient-specific topographies obtained from OCT or Scheimpflug imaging.

Third, the simulations were performed under idealised boundary conditions and excluded experimental noise or imaging uncertainty, which may influence deformation measurements in clinical practice. Integrating data assimilation techniques or uncertainty quantification frameworks could help address this limitation.

Finally, while the neural network provides interpretable coefficients that correlate with physical behaviour, it remains a data-driven model. The inclusion of Physics-Informed Neural Networks (PINNs) in future extensions of this work is expected to further constrain the model with governing physical laws, improving accuracy and robustness.

These enhancements will support broader clinical validation and facilitate the development of a patient-specific predictive tool for corneal biomechanical characterisation.

5 | CONCLUSION

This work represents a substantial advancement over our prior CFD–FSI modelling framework by introducing a dual-level surrogate approach that merges data-driven and physics-informed modelling. The Gradient Boosting Regressor efficiently reproduces air-puff pressure profiles previously obtained through CFD simulations, while the newly developed parametric neural network extends this capability to reconstruct spatial–temporal pressure and deformation patterns with interpretability and precision.

Estimating the air-puff pressure distribution on the cornea is crucial for enhancing the accuracy of intraocular pressure (IOP) measurements, which are vital for detecting and assessing corneal diseases. The precision of these measurements directly impacts the assessment of corneal material properties. While the fluid–structure interaction (FSI) method has shown high accuracy in predicting corneal compressive loads based on deformation, it requires extensive computational time, often up to 48 h. This study introduces a supervised machine learning (ML) regression algorithm designed to predict corneal pressure distribution from specific corneal parameters while optimising accuracy and reducing computational demand.

The primary outcome is a practical Gradient Boosting Regressor (GBR) model that effectively estimates corneal pressure distribution by accounting for key parameters: IOP, central corneal thickness (CCT), the corneal material coefficient (indicative of age), and the time step during testing. Our results reveal that air-puff pressure loading is significantly influenced by the intricate variations in corneal parameters unique to each patient. Additionally, the algorithm substantially decreases computational time from approximately 172,800 s (48 h) to 720 s (12 min)—a reduction of about 99.2%, while maintaining the accuracy

offered by the FSI model. This advancement in computational efficiency could greatly enhance the development of parametric equations for IOP and the Stress–Strain Index (SSI) by enabling analyses of a larger number of fully individualised eye models with dynamic topography, which will be the focus of our future research. Additionally, we propose incorporating Physics-Informed Neural Networks (PINNs) into the CFD-based air-puff model as part of our ongoing efforts. PINNs can leverage governing physical equations within the ML framework to provide faster and more accurate simulations, further reducing computational costs while enhancing the predictive capabilities of air-puff-based tonometry models. This innovative integration of PINNs has the potential to accelerate clinical workflows and improve the reliability of tonometry measurements in patient-specific applications.

This study introduces a neural network framework to model the pressure and deformation distributions on the corneal surface during air puff. By learning the relationships between input parameters (CCT, IOP, and μ_0) and five governing coefficients, the NN efficiently reconstructs high-fidelity CFD data. The results demonstrate the network's ability to capture shared temporal dynamics and distinct spatial patterns between pressure and deformation. Correlation analyses reveal dependencies of pressure and deformation on biomechanical inputs, showing the tailored parametric models. These findings establish the NN framework as a computationally efficient and interpretable tool for analysing fluid–structure interaction in ophthalmology. Future work will extend this framework to incorporate patient-specific geometries and dynamic boundary conditions for enhanced predictive capability.

Although the proposed model demonstrated stable performance across repeated runs and narrow statistical uncertainty, its validation on a limited number of clinical cases restricts conclusions about broad generalisability. In future work, we aim to validate the GBR+NN framework on larger multi-centre datasets encompassing a wider range of corneal geometries, dynamic topography and pathologies to confirm robustness and improve its applicability to real-world clinical tonometry.

ACKNOWLEDGEMENTS

The authors would like to thank the Leeds Institute for Fluid Dynamics for hosting the National Fellowships in Fluid Dynamics (NFFDY) 2024 summer programme funded by EPSRC, which formed the kick start of this work.

CONFLICT OF INTEREST STATEMENT

The authors declare no conflicts of interest.

ORCID

Osama M. Maklad https://orcid.org/0000-0001-6893-2654

Muting Hao https://orcid.org/0000-0001-5998-0021

REFERENCES

1. Weinreb, R. N., Leung, C. K. S., Crowston, J. G., Medeiros, F. A., Friedman, D. S., Wiggs, J. L., & Martin, K. R. (2016). Primary open-angle glaucoma. *Nature Reviews Disease Primers*, *2*(1),. https://doi.org/10.1038/nrdp.2016.67
2. Luce, D. A. (2005). Determining in vivo biomechanical properties of the cornea with an ocular response analyzer. *Journal of Cataract & Refractive Surgery*, *31*(1), 156–162.
3. Eliasy, A., Chen, K.-J., Vinciguerra, R., Lopes, B., Abass, A., Vinciguerra, P., Roberts, C., & Elsheikh, A. (2019). Determination of corneal biomechanical behavior in vivo for different ocular conditions using CorVis ST. *Journal of Cataract & Refractive Surgery*, *45*(6), 1040–1050.
4. Ambrósio, R., Valbon, B. F., Faria-Correia, F., Ramos, I., & Luz, A. (2013). Scheimpflug imaging for laser refractive surgery. *Current Opinion in Ophthalmology*, *24*(4), 310–320. https://doi.org/10.1097/icu.0b013e3283622a94
5. Rabinowitz, Y. S. (1998). Keratoconus. *Survey of Ophthalmology*, *42*(4), 297–319.
6. Ambrósio, Jr R., Correia, F. F., Lopes, B., Salomão, M. Q., Luz, A., Dawson, D. G., Elsheikh, A., Vinciguerra, R., Vinciguerra, P., & Roberts, C. J. (2017). Corneal Biomechanics in Ectatic Diseases: Refractive Surgery Implications. *The Open Ophthalmology Journal*, *11*(1), 176–193. https://doi.org/10.2174/1874364101711010176
7. Tonnu, P. A., Ho, T., Newson, T., El Sheikh, A., Sharma, K., White, E., Bunce, C., & Garway-Heath, D. The influence of central corneal thickness and age on intraocular pressure measured by pneumotonometry, non-contact tonometry, the Tono-Pen XL, and Goldmann applanation tonometry. *British Journal of Ophthalmology*, *89*(7), 851–854. https://doi.org/10.1136/bjo.2004.056622
8. Vinciguerra, R., Ambrósio, R., Elsheikh, A., Roberts, C. J., Lopes, B., Morenghi, E., Azzolini, C., & Vinciguerra, P. (2016). Detection of Keratoconus With a New Biomechanical Index. *Journal of Refractive Surgery*, *32*(12), 803–810. https://doi.org/10.3928/1081597x-20160629-01
9. Saad, A., & Gatinel, D. (2010). Topographic and Tomographic Properties of Forme Fruste Keratoconus Corneas. *Investigative Opthalmology & Visual Science*, *51*(11), 5546. https://doi.org/10.1167/iovs.10-5369
10. Elsheikh, A. (2010). Finite Element Modeling of Corneal Biomechanical Behavior. *Journal of Refractive Surgery*, *26*(4), 289–300. https://doi.org/10.3928/1081597x-20090710-01
11. Eliasy, A., Chen, K. J., Vinciguerra, R., Lopes, B. T., Abass, A., Vinciguerra, P., & Elsheikh, A. (2019). Determination of corneal biomechanical behavior in-vivo for healthy eyes using CorVis ST tonometry: Stress-strain index. *Frontiers in Bioengineering and Biotechnology*, *7*, 105. https://doi.org/10.3389/fbioe.2019.00105
12. Maklad, O., Eliasy, A., Chen, K. J., Theofilis, V., & Elsheikh, A. (2020). Simulation of air puff tonometry test using arbitrary Lagrangian–Eulerian (ALE) deforming mesh for corneal material characterisation. *International Journal of Environmental*

Research and Public Health, *17*(1), 54. https://doi.org/10.3390/ijerph17010054
13. Maklad, O., Eliasy, A., Chen, K. J., Wang, J., Abass, A., Lopes, B. T., Theofilis, V., & Elsheikh, A. (2020). Fluid-structure interaction based algorithms for IOP and corneal material behavior. *Frontiers in Bioengineering and Biotechnology*, *8*, 970. https://doi.org/10.3389/fbioe.2020.00970
14. Ariza-Gracia, M. Á., Wu, W., Calvo, B., Malvè, M., Büchler, P., & Rodriguez Matas, J. F. (2018). Fluid–structure simulation of a general noncontact tonometry. A required complexity? *Computer Methods in Applied Mechanics and Engineering*, *340*, 202–215. https://doi.org/10.1016/j.cma.2018.05.031
15. Vinciguerra, R., Rehman, S., Vallabh, N. A., Batterbury, M., Czanner, G., Choudhary, A., Cheeseman, R., Elsheikh, A., & Willoughby, C. E. (2019). Corneal biomechanics and biomechanically corrected intraocular pressure in primary open-angle glaucoma, ocular hypertension and controls. *British Journal of Ophthalmology*, *104*(1), 121–126. https://doi.org/10.1136/bjophthalmol-2018-313493
16. Roy, A. S., & Dupps, W. J. (2009). Effects of Altered Corneal Stiffness on Native and Postoperative LASIK Corneal Biomechanical Behavior: A Whole-eye Finite Element Analysis. *Journal of Refractive Surgery*, *25*(10), 875–887. https://doi.org/10.3928/1081597x-20090917-09
17. Yousefi, A., Roberts, C. J., & Reilly, M. A. (2022). The Shape of Corneal Deformation Alters Air Puff–Induced Loading. *Frontiers in Bioengineering and Biotechnology*, *10*. https://doi.org/10.3389/fbioe.2022.848060
18. Maklad, O. (2019). *Influence of fluid structure interaction on human eye biomechanics under air puff non-contact tonometry*. PhD thesis, University of Liverpool. https://ethos.bl.uk/OrderDetails.do?uin=uk.bl.ethos.778526
19. Yan, S., Hu, X., Song, X., Yao, K., & Qu, S. (2026). 结合有限元模拟和多层感知器神经网络模型的眼内压预测方法. *Acta Mechanica Sinica*, *42*(4),. https://doi.org/10.1007/s10409-025-24940-x
20. Sousa, P., Afonso, A., & Veiga Rodrigues, C. (2024). Application of machine learning to model the pressure poisson equation for fluid flow on generic geometries. *Neural Computing and Applications*, *36*(26), 16581–16606. https://doi.org/10.1007/s00521-024-09935-0
21. Gupta, R. (2022). *Deep learning-based reduced order modeling for unsteady flow dynamics and fluid-structure interaction*. University of British Columbia. https://doi.org/10.14288/1.0406379
22. Hassan, K., Dayoub, I., Hamouda, W., & Berbineau, M. (2010). Automatic modulation recognition using wavelet transform and neural networks in wireless systems. *EURASIP Journal on Advances in Signal Processing*, *2010*(1). https://doi.org/10.1155/2010/532898
23. Friedman, J. H., Tibshirani, R., & Hastie, T. (2000). Additive logistic regression: A statistical view of boosting (with discussion and a rejoinder by the authors). *The Annals of Statistics*, *28*(2), 337–407. https://doi.org/10.1214/aos/1016120463
24. Desouky, N. A., Saafan, M. M., Mansour, M. H., & Maklad, O. M. (2023). Patient-specific air puff-induced loading using machine learning. *Frontiers in Bioengineering and Biotechnology*, *11*. https://doi.org/10.3389/fbioe.2023.1277970
25. Elsheikh, A., Geraghty, B., Rama, P., Campanelli, M., & Meek, K. M. (2010). Characterization of age-related variation in corneal biomechanical properties. *Journal of the Royal Society Interface*, *7*(51), 1475–1485. https://doi.org/10.1098/rsif.2010.0108
26. Friedman, J. H. (2001). Greedy function approximation: A gradient boosting machine. *The Annals of Statistics*, *29*(5), 1189–1232. https://doi.org/10.1214/aos/1013203451
27. Scikit-Learn Developers. (2023). Gradient Tree Boosting – GradientBoostingRegressor. Retrieved from https://scikit-learn.org/stable/modules/generated/sklearn.ensemble.GradientBoostingRegressor.html

SUPPORTING INFORMATION

Additional supporting information can be found online in the Supporting Information section at the end of this article.

How to cite this article: Maklad, O. M., & Hao, M. (2026). Reduced order modelling of air-puff test for corneal material characterisation. *Journal of Microscopy*, 1–19. https://doi.org/10.1111/jmi.70077